

In-Situ Surface Roughness Measurement of Laser Beam Melted Parts – a Feasibility Study of Layer Image Analysis

Joschka zur Jacobsmühlen*¹, Stefan Kleszczynski², Alexander Ladewig³, Gerd Witt², Dorit Merhof¹

¹ Institute of Imaging and Computer Vision, RWTH Aachen University, Aachen, Germany

² Institute for Product Engineering, University of Duisburg-Essen, Duisburg, Germany

³ MTU Aero Engines AG, Munich, Germany

* Corresponding Author: joschka.jacobsmuehlen@lfb.rwth-aachen.de, +49 241 80-27974

Abstract

Laser Beam Melting (LBM) systems produce three-dimensional parts from metal powder by iteratively melting the top layer of a powder bed according to the sliced part geometry and applying a new powder layer. LBM enables the production of complex geometries with mechanical properties suitable for industrial application. The adoption of LBM in application areas with high quality requirements, such as aerospace or medical requires thorough quality assurance methods, which are a current research topic. The measurement of surface roughness is time-consuming and cannot be performed on internal part surfaces, e.g. channels. We acquire high resolution layer images (20...30 $\mu\text{m}/\text{pixel}$) of the melt result of experimental build jobs and develop an in-situ method for surface roughness measurement. Part contours are segmented in each layer and surface profiles are reconstructed from successive layers. From these surface profiles the same surface roughness measures as in physical measurements are computed. Reference measurements are obtained by profilometry and compared to the image-based results. Our measurements fail to reproduce the mechanical measurement results, which may be due to insufficient image resolution or roughness deviations caused by melt extensions below the current build layer.

1 Introduction

Laser Beam Melting (LBM) is an Additive Manufacturing method, which produces parts from metal powder by selectively melting the sliced geometry of a part in a powder bed. After the laser exposure, the build platform is lowered and a new powder layer is deposited. The process is repeated until the entire part is built. LBM enables the production of complex (e.g. bionical designs) and individual components, which is highly desirable for aerospace applications. This is why MTU Aero Engines AG has established a first LBM production line. To ensure perfect part quality, different approaches are used which cover the whole process chain and provide destructive and non-destructive testing of materials, qualification of process parameters and online process monitoring [1].

The surface roughness of parts produced by LBM is a part property which is often the target of optimization, as poor surface quality requires additional post-processing steps which are time-consuming and may be impossible, e.g. for internal structures/channels. Previous work therefore focuses on minimizing surface roughness or investigating dependencies between roughness and process parameters. Yasa and Kruth [2] minimized the surface roughness by re-melting the part layers. Strano et al. [3] developed a computational model for the surface roughness with respect to the process parameters. Vetterli et al. [4] compared four

different measurement methods for laser-sintered parts including a novel photometric stereo method. In all of these works the measurements are performed using profilometry and/or 3D imaging *after* the build process has finished. An inline method for 3D surface metrology which is integrated into the machine's laser path and utilizes optical coherence tomography is presented in [5]. The extracted 3D surface allows measuring the surface roughness of a layer after laser exposure but does not consider the part contours, which will form the surface of the finished part.

An in-situ measurement is highly desirable to inspect surface roughness for produced parts and ensure fulfilment of design requirements. In this work we analyze high resolution layer images from a series of experimental build jobs for which mechanical surface roughness measurements were performed. We replicate the steps of a physical roughness measurement using layer image data to investigate whether an in-situ measurement of surface roughness based on images is feasible.

2 Methods

Conventionally, surface roughness is measured using a stylus which is moved across the part's surface to extract a surface profile. This profile is then filtered to differentiate shape deviations (low-frequency components) and surface roughness (high-frequency

components). Our image analysis pipeline replicates the physical procedure: after layer image acquisition, the part contours are segmented and surface profiles are created from which we extract the image-based roughness information. The following sections describe these steps in detail.

2.1 Experimental Setup

We tested our method on multiple build jobs of a twelve-sided hollow frustum of a pyramid, which was built on an EOSINT M 270 system by EOS GmbH, Germany using EOS NickelAlloy IN718 powder. In order to generate ground truth measurements, surface roughness was measured according to DIN EN ISO 4287/4288 [6], [7] by a Mitutoyo SJ-400 profilometer for three segments per side (Figure 1). We divide each roughness profile $y(x)$ into five segments $y_i(x)$ and compute the mean roughness depth R_{zDIN} :

$$R_z(i) = \max y_i(x) - \min y_i(x) \quad (1)$$

$$R_{zDIN} = \frac{1}{5} \sum_{i=1}^5 R_z(i) \quad (2)$$

which is then averaged over all three segments yielding \bar{R}_{zDIN} for each pyramid face. We build our test geometry nine times and obtain 216 ground truth measurements of \bar{R}_{zDIN} .

2.2 Image Acquisition

All experimental build jobs were documented using a high resolution imaging system (20...30 $\mu\text{m}/\text{px}$) which acquires layer images of the powder bed and the melt result for each layer in the build job [8]. A monochrome CCD camera (SVS29050M, SVS-Vistek GmbH, Germany) with an image resolution of 6576×4384 px in combination with a tilt and shift lens (120 mm Superrotator, Hartblei, Germany) is attached to the machine window (Figure 2), the image acquisition is triggered by limit switch signals of the machine's recoater blade. Image size after perspective correction is approximately 3000×3000 px. An LED line placed below the machine windows provides indirect lighting by using the machine back as reflector.

2.3 Part Contour Segmentation

The segmentation of part contours in high resolution layer images is a difficult task since the metal powder appears as a noise-like background in the image and the part boundaries do not stand out against the surrounding powder regions (Figure 3). We therefore use a-priori information from each part's layer geometries to limit the region of interest for segmentation around the part contour. We import the part geometries from Common Layer Interface (CLI) files and extract the part contour polygons.

In preliminary experiments we tried to refine these

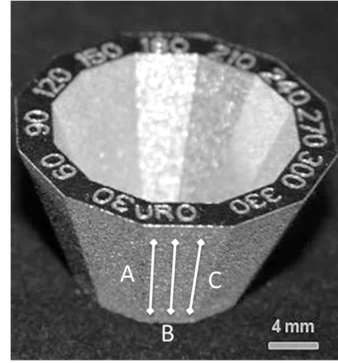


Figure 1: Test geometry (frustum of a twelve-sided hollow pyramid, 5 mm walls, 45° overhanging angles) and sample measurements for one surface

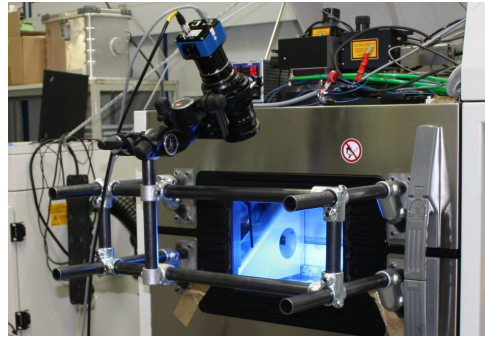


Figure 2: Camera setup in front of machine window

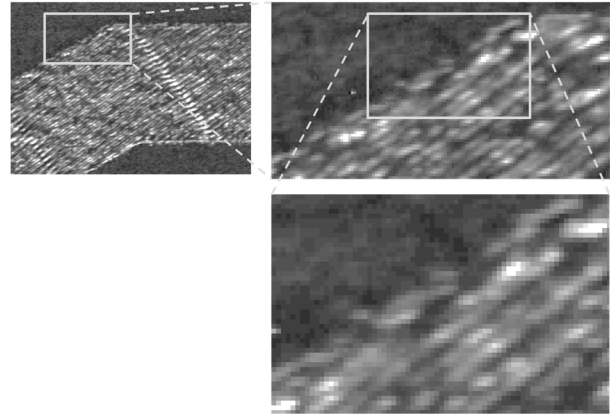


Figure 3: Example of contour segmentation region

contour polygons by moving each point (in discrete coordinates) along the contour normal to the edge position detected by an 1D edge detector. This failed due to positions with low contrast. Active contours (“snakes”) or level-set based methods (Chan-Vese) are too slow for our high resolution images (~9 Megapixel) due to the iterative solution. Additionally, the choice of parameters is difficult for part contours with many sharp bends which are segmented as smooth curves. Additional contour constraints for these bends help to improve the

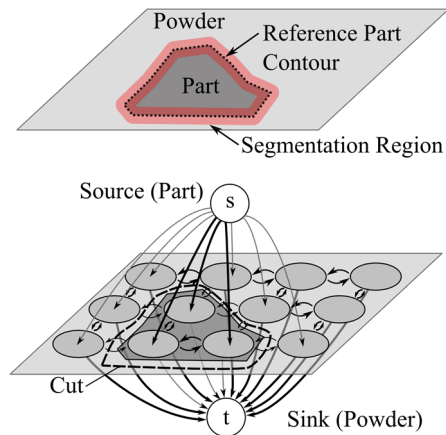


Figure 4: Graph Cuts segmentation. Top: definition of segmentation region S , bottom: min-cut result

segmented shape but in turn lead to higher segmentation error due to the reduced contour flexibility. Hence we use 2D edge detection to extract as much information about the part boundary as possible. Since small gradient operators such as the Sobel operator lead to many falsely detected edges in the noise-like powder regions, we select steerable filters [9] and Structured Forests for Edge Detection [10] which are robust against local small scale intensity changes.

Since detected edges still exhibit gaps as well as many weak edges which do not belong to part contours we consider a global optimization of region boundaries based on the Graph Cuts method [11].

Graph Cuts finds an optimum region partitioning by representing image pixels as nodes in a graph which are connected to a source terminal (part) and a sink terminal (powder). The edges between nodes and terminals and between neighboring nodes are assigned different weights and Graph Cuts computes a solution which maximizes the flow between the source terminal and the sink terminal [11]. Edges with small flow are cut, forming two regions associated with source/part and sink/powder (Figure 4). We define a segmentation region S around the reference contour. Part regions which do not overlap with S are only connected to the source, powder regions which do not overlap with S are only connected to the sink (Figure 4). The assignment is kept during the segmentation.

As we want the region boundaries to follow the detected edges, the edge weights (pixel similarity) between neighboring pixels are initialized with a constant value and then reduced if a neighboring pixel belongs to a detected edge to increase the probability of a cut between these pixels. The final contour is obtained as the boundary of the segmented foreground region after application of the min-cut/max-flow algorithm [11].

2.4 Multiscale Edge Detection + Graph Cuts

Our first variant of edge detection and Graph Cuts segmentation uses multiscale edge detection based on steerable filters [9]. We perform edge detection for multiple scales ($\sigma = 1, 2, 4$) with non-maximum suppression and extract the strongest five percent of edges which intersect with the segmentation region S at each scale. The final edge map is obtained as the sum of all scale edge maps and normalized to the interval $[0, 1]$.

2.5 Structured Forests Edge Detection + Graph Cuts

The second variant is based on Structured Forests for Edge Detection [10] which utilize structured learning to learn an edge detector that predicts local edge masks from image patches. It uses a Random Forest classifier and yields a soft decision edge map image. We have found it to be very robust to the noise-like image structure of powder regions. The prediction is based on color, gradient magnitude and gradient orientation. To exploit the a-priori information of our reference geometry masks, we combine layer images with two different lightings and the reference geometry mask into a three-channel “color” image, which is then processed by the edge detector. We use the multiscale detector (denoted as SE-MS in [10]) with four trees and non-maximum suppression for edge thinning.

2.6 Evaluation of Contour Segmentation

To obtain a reference segmentation we manually traced the part contours in four layer images and compared our segmentation results to this ground truth. As we are interested in the absolute local distances between segmented contour and ground truth,

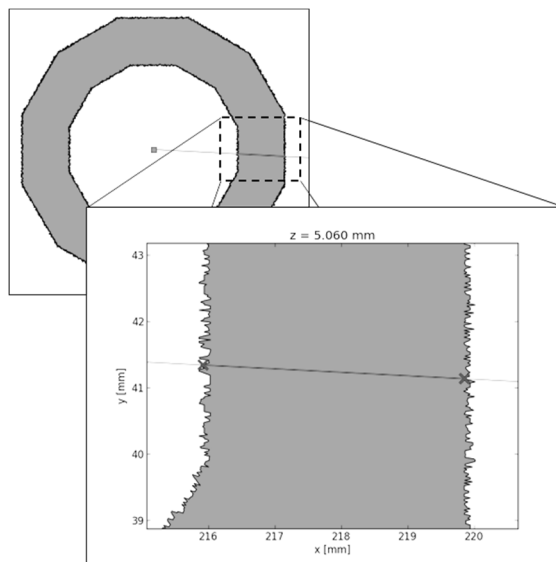


Figure 5: Extraction of surface profiles for internal and external surface

we utilize the bidirectional local distance measure [12], which computes a meaningful local distance for each point of the reference contour even for complex shapes.

2.7 Surface Profile Reconstruction and Roughness Measurement

The mechanical measurements on our test geometry were performed on the interior and exterior of each pyramid face; we therefore extract an internal and external surface profile by intersecting radial rays with the segmented contours in each layer (Figure 5) and by combining the intersection points. Rays are placed at angles of $\alpha = 0^\circ, 30^\circ, \dots, 330^\circ$. The obtained profiles are discrete with a point spacing of $20 \mu\text{m}$ (layer height) in z -direction; as we only extract peak-to-peak statistics this is not critical.

The form deviations are computed by subtracting the reference CLI geometry from the extracted profiles (Figure 6). Then, the roughness profile is computed by applying a highpass filter as defined in ISO 16610-21 (Figure 7). For each pyramid face we measure the roughness on three segments (cf. Figure 1) at $\alpha, \alpha \pm 3^\circ$ and compute the mean roughness depth \bar{R}_{zDIN} which is then displayed for all faces in a polar plot (Figure 8).

2.8 Validation of Measurements

We validate our image-based measurements against the results obtained by profilometry. As the surface roughness of parts with overhanging geometries depends on the part position inside the process chamber and is increased for surfaces which face the walls of the process chamber [13], these deviations should be present in the image-based measurements, too. For qualitative analysis we divide the results of each roughness measurement (external/internal and reference/image-based) by its largest value to obtain a normalized roughness measurement between zero and one and plot them in the same axis for visual comparison.

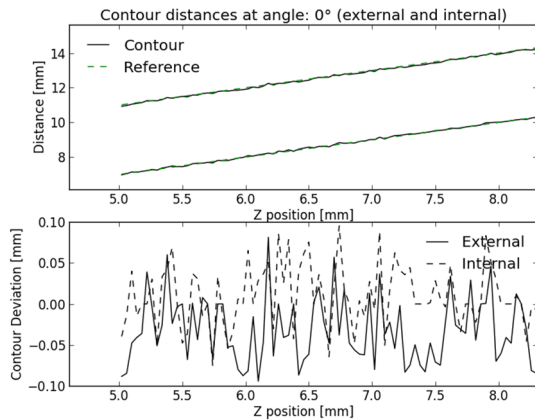


Figure 6: Extraction of contour deviations. Top: distance to part center, bottom: subtracting the reference contour distances yields contour deviations

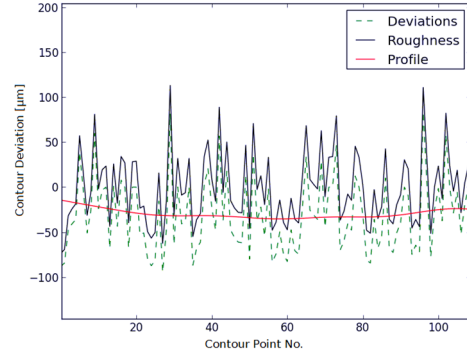


Figure 7: Separation of contour deviations into profile and surface roughness using highpass filter

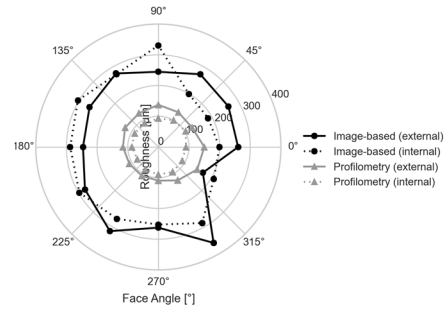


Figure 8: Roughness measurement results from layer image analysis and profilometry for external and internal part surfaces.

3 Results

The results of the contour segmentation evaluation are displayed in Figure 9 for four layer images. The combination of Structured Forests edge detection with Graph Cuts segmentation achieves a lower median error of $27.7 \mu\text{m}$ (MS+GC: $39.1 \mu\text{m}$) and is robust to difficult images ($z = 11.0 \text{ mm}$). Consequently, we select this combination for all subsequent analysis steps.

Figure 8 shows an exemplary result of the image-based surface roughness measurement and the reference values from profilometry. Image analysis generally yields larger values which do not match the reference.

We analyze the distribution of the difference between \bar{R}_{zDIN} and the results of our image analysis in Figure 11 (left).

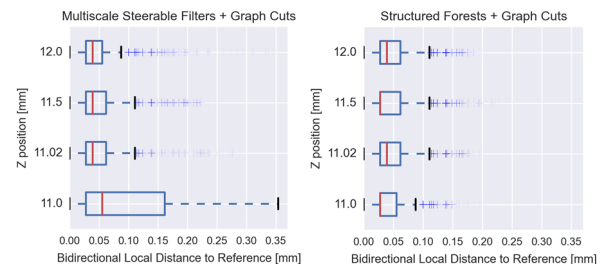


Figure 9: Evaluation of contour segmentation against manual segmentation

The median error for all 216 measurements is 131.3 μm , which is very high with respect to the reference values which are in the order of 70...160 μm .

The normalized roughness measurements are displayed in Figure 10. The characteristic deviations, e.g. in the first row (top right) at 0° or in the second row (center left) at 135° are not well reproduced by the normalized image-based measurements. We summarize the difference between the normalized roughness measurements in Figure 11 (right). Most normalized roughness values from image analysis are too low as indicated by the negative error and the median difference of -0.135. This suggests that some roughness values from the image analysis are too high and reduce the normalized values at other positions.

4 Discussion

The results of our analysis show that the image-based surface roughness measurements do not precisely match mechanical measurement acquired by a profilometer. While a different scale of measurement results could be fixed by calibrating the setup, the missed roughness deviations indicate that the image-based approach does not capture the structures causing the surface roughness of produced parts. A possible cause is the image resolution which ranges from 20-30 $\mu\text{m}/\text{pixel}$ (depending on the field of view) while the magnitude of position-dependent surface roughness deviations is in the order of 20-50 μm making the deviations hard to resolve for the image-based method.

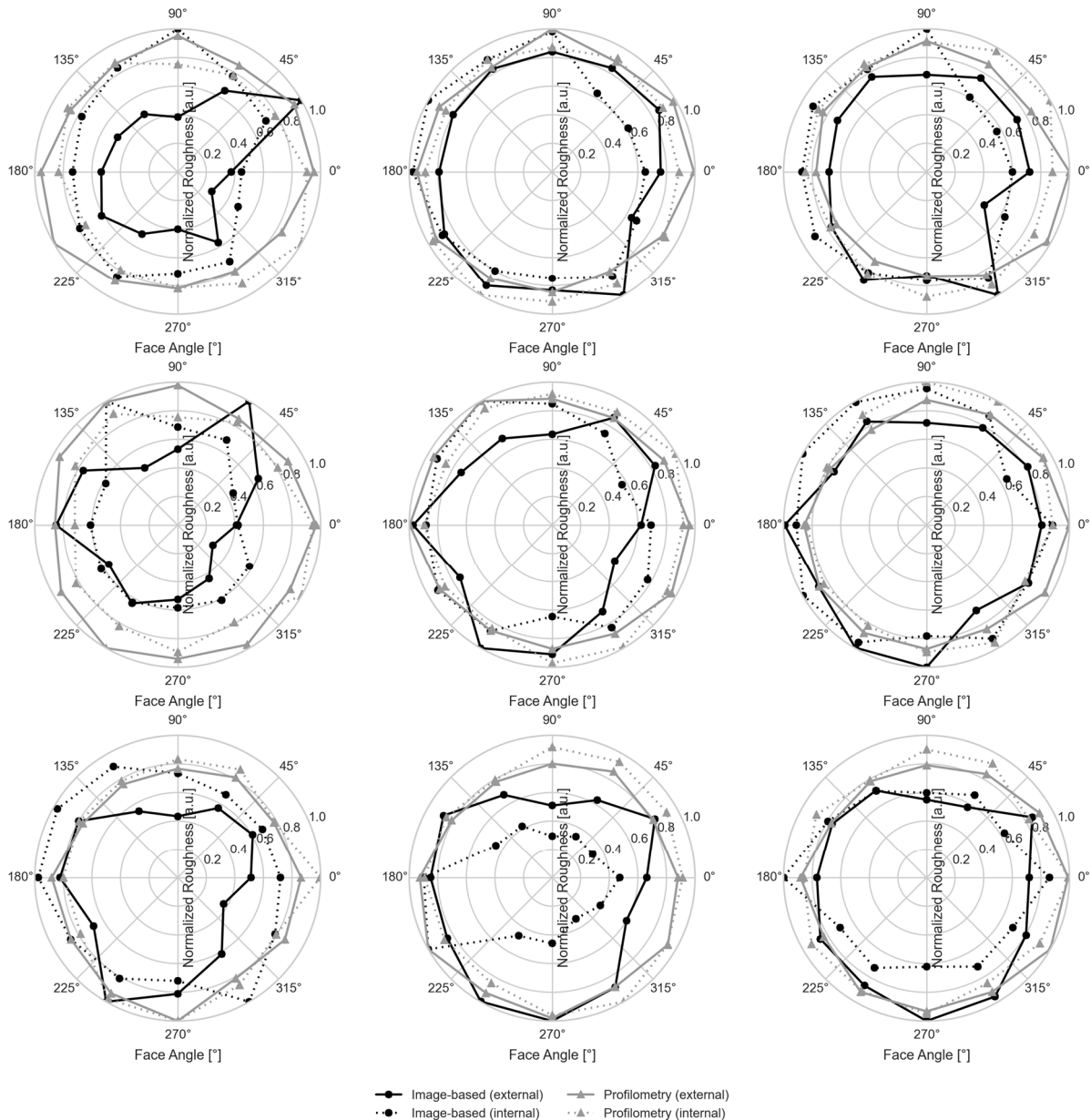


Figure 10: Normalized roughness for all specimens obtained from image analysis (black) and profilometry (gray)

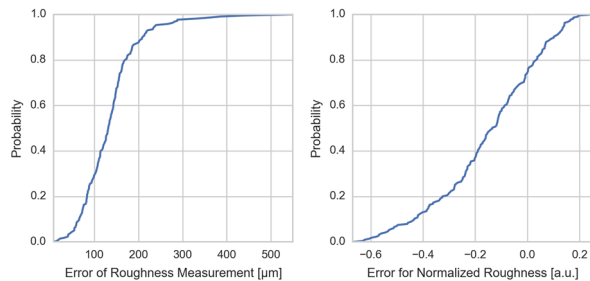


Figure 11: Empirical cumulative distribution function of measurement error. Left: compared to profilometry reference, right: comparison of normalized roughness values.

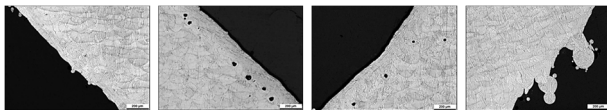


Figure 12: Micrographs of test specimen (from [13]), the external surface on the left is smooth while the surface on the right exhibits melt extensions.

The median segmentation error of $27.7 \mu\text{m}$ is possibly too high to correctly capture the small-scale contour information. This is partly due to the lighting which was optimized for inspection of the reflective part surfaces (where glare has to be avoided) and not for optimum contrast around the part contours.

In [13] micrographs of specimens with overhanging structures are presented (Figure 12) that show melt extensions on the outer surfaces which are considered a probable cause of the position-dependent roughness deviations. As these melt extensions appear below the current build layer, they cannot be captured by acquiring images of the current (top) build layer. If these effects cause the surface roughness deviations, an increased image resolution would not be helpful, either.

5 Conclusion

We have developed an image-based method for in-situ measurement of surface roughness. Our analysis replicates the steps of physical roughness measurements and extracts surface profiles from contour segmentations of subsequent layer images. The evaluation of experimental results showed high measurement errors compared to the reference measurements by profilometry, thus disqualifying the image-based method for direct quantitative measurements.

Literature

[1] G. Zenzinger, J. Bamberg, A. Ladewig, T. Hess, B. Henkel, and W. Satzger, "Process monitoring of additive manufacturing by using optical tomography," *AIP Conference Proceedings*, vol. 1650, pp. 164–170, 2015.

[2] E. Yasa and J. Kruth, "Application of Laser Re-Melting on Selective Laser Melting Parts," *Advances in Production Engineering & Management*, vol. 6, no. 4, pp. 259–270, 2011.

[3] G. Strano, L. Hao, R. M. Everson, and K. E. Evans, "Surface roughness analysis, modelling and prediction in selective laser melting," *Journal of Materials Processing Technology*, vol. 213, no. 4, pp. 589–597, 2013.

[4] M. Vetterli, M. Schmid, and K. Wegener, "Comprehensive investigation of surface characterization for laser sintered parts," in *Fraunhofer Direct Digital Manufacturing Conference 2014*, 2014.

[5] R. Schmitt, T. Pfeifer, and G. Mallmann, "Machine integrated telecentric surface metrology in laser structuring systems," *ACTA IMEKO*, vol. 2, no. 2, pp. 73–77, 2013.

[6] *Geometrical Product Specifications (GPS) – Surface texture: Profile method – Terms, definitions and surface texture parameters (ISO 4287:1997 + Cor 1:1998 + Cor 2:2005 + Amd 1:2009); German version EN ISO 4287:1998 + AC:2008 + AI:2009*. ISO, 1998.

[7] *Geometrical Product Specifications (GPS) – Surface texture: Profile method – Rules and procedures for the assessment of surface texture (ISO 4288 : 1996); German Version EN ISO 4288 : 1997*. ISO, 1998.

[8] J. zur Jacobsmühlen, S. Kleszczynski, D. Schneider, and G. Witt, "High resolution imaging for inspection of Laser Beam Melting systems," in *IEEE International Instrumentation and Measurement Technology Conference (I2MTC) 2013*, 2013, pp. 707–712.

[9] M. Jacob and M. Unser, "Design of steerable filters for feature detection using canny-like criteria," *Pattern Analysis and Machine Intelligence, IEEE Transactions on*, vol. 26, no. 8, pp. 1007–1019, 2004.

[10] P. Dollár and C. L. Zitnick, "Structured Forests for Fast Edge Detection," in *Computer Vision (ICCV), 2013 IEEE International Conference on*, 2013, pp. 1841–1848.

[11] Y. Boykov and V. Kolmogorov, "An experimental comparison of min-cut/max-flow algorithms for energy minimization in vision," *Pattern Analysis and Machine Intelligence, IEEE Transactions on*, vol. 26, no. 9, pp. 1124–1137, 2004.

[12] H. S. Kim, S. B. Park, S. S. Lo, J. I. Monroe, and J. W. Sohn, "Bidirectional local distance measure for comparing segmentations," *Medical Physics*, vol. 39, no. 11, pp. 6779–6790, 2012.

[13] S. Kleszczynski, A. Ladewig, K. Friedberger, J. zur Jacobsmühlen, D. Merhof, and G. Witt, "Position Dependency of Surface Roughness in Parts from Laser Beam Melting Systems," in *Proceedings of the 26th International Solid Free Form Fabrication (SFF) Symposium*, 2015.